Journal Pre-proof

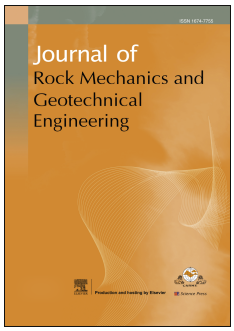

Moment tensor inversion of mining-induced seismic events and forward modeling of critical fault slip to prevent rockbursts

Jiefang Song, Caiping Lu, Arno Zang, Derek Elsworth, Xiufeng Zhang, Qingxin Qi, Chunhui Song

PII: S1674-7755(24)00295-6

DOI: https://doi.org/10.1016/j.jrmge.2024.07.001

Reference: JRMGE 1621

To appear in: *Journal of Rock Mechanics and Geotechnical Engineering*

Received Date: 12 January 2024

Revised Date: 25 June 2024

Accepted Date: 10 July 2024

Please cite this article as: Song J, Lu C, Zang A, Elsworth D, Zhang X, Qi Q, Song C, Moment tensor inversion of mining-induced seismic events and forward modeling of critical fault slip to prevent rockbursts, *Journal of Rock Mechanics and Geotechnical Engineering*, https://doi.org/10.1016/j.jrmge.2024.07.001.

Moment tensor inversion of mining-induced seismic events and forward modeling of critical fault slip to prevent rockbursts

Jiefang Song [a], Caiping Lu [a, *], Arno Zang [b], Derek Elsworth [c], Xiufeng Zhang [d], Qingxin Qi [e], Chunhui Song [a]

[a] Key Laboratory of Deep Coal Resource Mining (Ministry of Education), School of Mines, China University of Mining and Technology, Xuzhou, 221116, China

[b] Helmholtz Centre Potsdam, GFZ German Research Centre for Geosciences, Potsdam, 14473, Germany

[c] Department of Energy and Mineral Engineering, EMS Energy Institute and G3 Center, Pennsylvania State University, University Park, PA, 16802, USA

[d] Center of Rockburst Prevention Research, Shandong Energy Group, Jinan, 250101, China

[e] Deep Mining and Rockburst Research Institute, Chinese Institute of Coal Science, Beijing, 100013, China

* Corresponding author. E-mail address: cplu@cumt.edu.cn (C.P. Lu).

Abstract: In this study, we employed Bayesian inversion coupled with the summation-by-parts and simultaneous-approximation-term (SBP-SAT) forward simulation method to elucidate the mechanisms behind mining-induced seismic events caused by fault slip and their potential effects on rockbursts. Through Bayesian inversion, it is determined that the sources near fault FQ14 have a significant shear component. Additionally, we analyzed the stress and displacement fields of high-energy events, along with the hypocenter distribution of aftershocks, which aided in identifying the slip direction of the critically stressed fault FQ14. We also performed forward modeling to capture the complex dynamics of fault slip under varying friction laws and shear fracture modes. The selection of specific friction laws for fault slip models was based on their ability to accurately replicate observed slip behavior under various external loading conditions, thereby enhancing the applicability of our findings. Our results suggest that the slip behavior of fault FQ14 can be effectively understood by comparing different scenarios.

Keywords: Rockburst; Fault slip; Moment tensor inversion; Friction law

1. Introduction

Study of rock mass response during fault slip has played a crucial role in dynamic disaster prevention in coal mines, particularly given the frequent occurrence of rockbursts near pre-existing faults (Dou et al., 2014; Keneti and Sainsbury, 2018; Duan et al., 2022). Tremors induced by fault instability primarily stem from mining-induced stress perturbations. These tremors are distinguished from other sources by their release of more energy, which poses significant destructive potential to roadway structures (Zhang et al., 2022). A major rockburst accident involving a fault slip occurred on 20 October 2018, in Shandong Province, China, resulting in 21 fatalities (Song et al., 2023). This incident prompted an investigation into the mechanisms governing rockbursts and strategies for preventing them in the future.

Rockbursts and mining-induced tremors are gaining increased attention in fault zones (Zhou et al., 2022), as they can amplify the seismic response (Guo et al., 2022; He et al., 2022; Cao et al., 2023). In principle, the physical processes of natural earthquakes and mining-induced tremors exhibit similarities (Kwiatek et al., 2011; Zhang et al., 2023). Although the magnitude of these tremors induced in coal mines is relatively small (typically with M_L values ranging between 0 and 1.5) compared to natural earthquakes. This is due to the limited volumes of rock mined-out during mining operations, which directly affects the degree of stress transfer and release.

Research on mining-induced fault slip primarily focuses on three aspects: (1) understanding the focal mechanisms of mining-induced tremors caused by fault slip (Mendecki et al., 2020), (2) investigating how mining operations affect stress transfer and microseismic (MS) activity near faults (Kozłowska et al., 2021), and (3) analyzing the response characteristics and instability mechanisms of roadways under the influence of tremors (Sainoki and Mitri, 2014). These research topics typically utilize a combination of field analyses (Lu et al., 2019; Jiang et al., 2020), laboratory experiments (Deng et al., 2018; Li et al., 2019), and numerical simulations (Gao et al., 2021). Additionally, moment tensor inversion (MTI) technology is the most effective approach for analyzing the kinematics of fractures at both field and laboratory scales. MTI can accurately determine source-related parameters of tremors, including scalar moment, components contribution, and fault plane parameters (e.g. strike, dip and rake). In particular, focal mechanism solutions can serve as input for the stress inversion routine to explore stress orientations within the fault zone (Dufumier and Rivera, 1997; Petružálek et al., 2020; Song et al., 2022). However, there has been relatively limited exploration into integrating these detailed source parameters into numerical

models for a comprehensive analysis of fault instability mechanisms.

MTI methods assist in understanding the mechanism of sources behind complex phenomena (Martínez-Garzón et al., 2016a, b). Different types of seismic data, such as seismic waveforms, first-motion polarity data and amplitude spectra/ratios, can be used individually or in combination to extract earthquake kinematics. Each approach has its distinct advantages and limitations (Hamidbeygi et al., 2023). First-motion inversion requires stations to be clustered around and close to the source with good coverage of the focal sphere (Iwata, 2018; Braunmiller et al., 2020). However, this method faces challenges when dealing with low-energy events due to signal-to-noise ratio limitations. Full-waveform inversion offers a more comprehensive dataset by incorporating a prior velocity model tailored to the local environment, thereby fitting observed data with a specified signal-to-noise ratio effectively (Ma et al., 2018). Moreover, building Green's function at high frequencies is complicated (Bentz et al., 2018). The amplitude spectrum discards polarity information during the inversion process, which reduces the likelihood of determining accurate fault plane information (Cesca et al., 2006). MTI techniques can also partition the shear and volumetric strain components (Wang et al., 2017a, b), and integrating these results with forward simulation has proven effective for analyzing fault kinematics (Meng et al., 2022; Wang and Luan, 2022). Most studies replicate the propagation of seismic waves in elastic solid media based on the elasto-dynamic wave equation, but building a realistic source model remains challenging (Bai et al., 2021). With the development and accessibility of high-performance computing, forward simulations based on elasto-dynamic response are becoming prevalent (Feng et al., 2015; Zhang et al., 2019). This method effectively reveals the propagation of seismic waves and fault rupture processes with focal mechanisms as inputs within complex underground structures (Gao et al., 2021; Zhang et al., 2024). The seismic source models for fault modeling can be categorized into point source and finite fault source models (Dang et al., 2020). Accurately simulating fault rupture, especially the stick-slip process on finite faults, requires appropriate frictional properties (Latour et al., 2011; Hu et al., 2017; Luo and Duan, 2018; He et al., 2020; Im and Avouac, 2022). Presently, there are few numerical codes capable of yielding finite source model results at mine scale. Fault slip involves shear on fractures that spontaneously propagate along a frictional interface within an elastic or bimaterial solid. Moreover, fault instability exhibits different behaviors under varying geological conditions. However, limited research has been conducted on this phenomenon specifically in the context of mining-induced stress disturbances.

In this study, we aim to address these documented gaps in current understanding by conducting a comprehensive analysis of fault slip behavior and its implications for mining hazard prevention. First, we utilize MTI to analyze the rupture modes of high-energy seismic events within the fault region. Building upon field observations, we proceed to forward simulation of pure-shear slip on faults, considering various slip modes and friction laws. Finally, we interpret our model results in the context of faulting and propose mining hazard mitigation strategies based on comparisons with field observations. By critically evaluating and integrating these aspects, our study aims to deepen understanding of fault instability mechanisms and identify key controlling variables and their implications for mining safety.

2. Site characteristics

The study focuses on seismic events monitored in the Dongtan coal mine in China at the depths ranging between 520 m and 700 m. The 3308 working face is located in District No. 3 of the Dongtan coal mine (depth range from 538.5 m to 623.7 m). The unmined area lies to the north, with the 3307 goaf (April 2020) to the south, separated by a remaining coal pillar 4.5 m in width (Fig. 1). The No. 1 Xiaochang fault (throw = 0-17 m) and the boundary coal pillar are located to the west of the mine, close to the 5319 (abandoned in March 2000) and 5320 goafs (abandoned in December 2002) of the adjacent Xinglongzhuang coal mine (Fig. 1, upper right inset). The headgate and tailgate of the working face are located on parallel roadways, with the north and south roadways serving as the headgate and tailgate, respectively. The 3308 working face is accessed by inclined roadways, including tailgate (1629 m), headgate (1639 m) and cuttergate (364 m). Above the coal seam is a thick layer of hard sandstone. The immediate roof consists of siltstone with an average thickness of 2.9 m, while the main roof is composed by fine sandstone with an average thickness of 23.5 m. The immediate and main floors are siltstone and fine sandstone, with thicknesses of 1.2 m and 9.9 m, respectively. The presence of the hard-thick roof stratum significantly impacts the mining-induced stress transfer and consequently the occurrence of tremors.

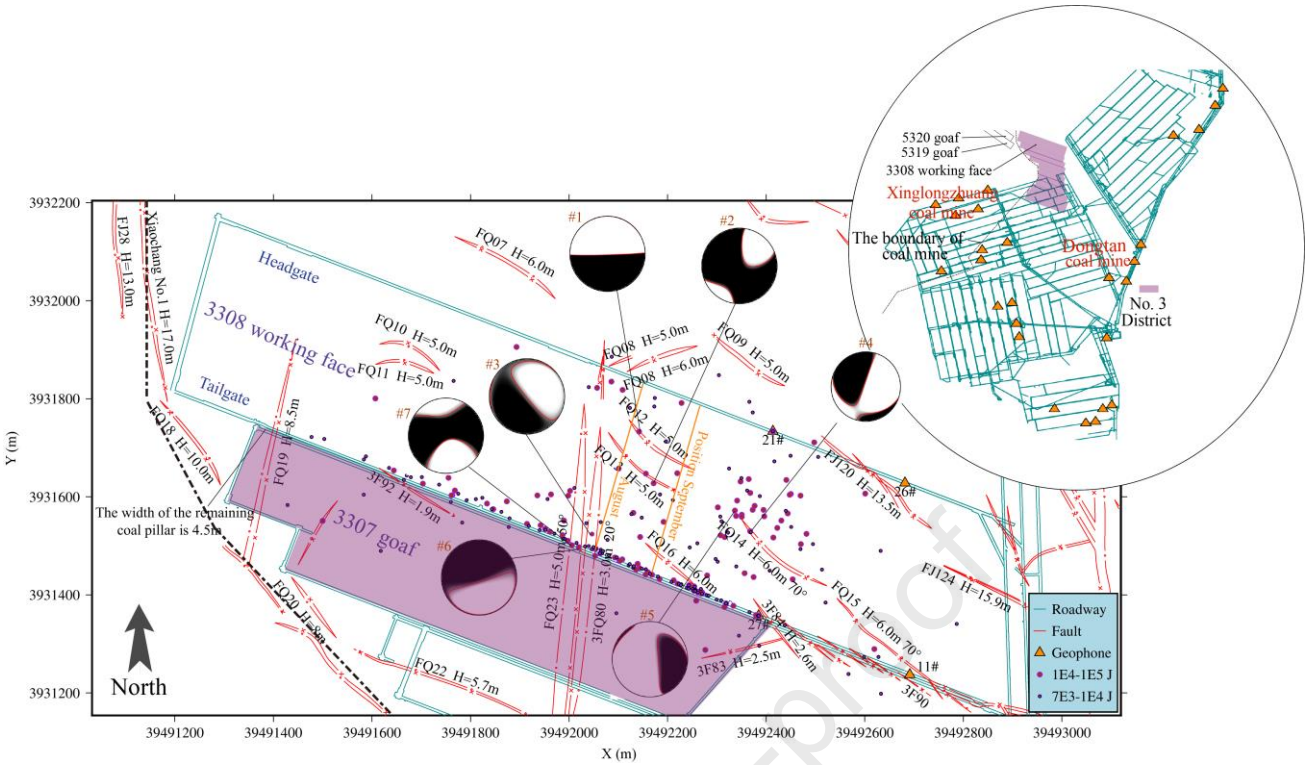

Fig. 1. Location of high-energy mining-induced tremors in relation to faults and layout of working face roadways. The black and white circles represent fault plane solutions of individual high-energy events near faults. The image in the upper-right corner shows the overall layout of the mine roadway including the locations of the geophones array used for detecting seismic tremors. Small dots indicate MS event locations with two levels of color-coded seismic radiated energy values (events occurred from 1 May 2022 to 31 August 2022). The two orange lines depict the mining positions of the working face in August 2022 and September 2022, respectively.

This coal mine has experienced two rockburst incidents, occurring on 1 June 2001 and 3 January 2005, both attributed to mining-induced modulation of tectonic stress. Within the 3308 working face, there are 21 mature faults, which have served as catalysts for numerous high-energy induced events during mining operations, with a maximum recorded energy reaching 3.8×10^4 J (refer to Table A1 in Appendix A). Notably, 15 of these faults (see Fig. 1) exhibited throws larger than 3 m. Among them, seven faults are located within 3308 working face, including FQ16 (0-6 m), FQ14 (0-6 m), and FJ124 (15.9 m). Currently, the FQ23, 3FQ80, FQ12 and FQ13 faults have been traversed, with the subsequent mining phase targeting the FQ14 fault. The potential activation or instability of this fault poses significant safety concerns. Additionally, the coal exhibits an elastic energy index of 2.74 and a uniaxial compressive strength of 9.7 MPa (see Fig. A2 in Appendix A). The combined factors of the stiff and strong over/underburned, high burial depth, and low-strength brittle coal create critically conducive conditions for triggering rockbursts on the FQ14 fault. Hence, it is crucial to explore the rupture mechanism of the FQ14 fault and employ forward modeling to identify potential failure modes under mining-induced stress. This analysis will help develop effective strategies to mitigate the hazard.

3. Methods

In this section, we describe the Bayesian MTI methods used to obtain source information for tremors. We employ a shear slip model to compute further slip of a selected fault using two constitutive friction laws. The MTI (first-motion polarity) results guide the selection of fracture types for the numerical simulation of the FQ14 fault.

3.1. Bayesian MTI (first-motion polarity)

MTI is a well-known technique and can be represented as

$$\boldsymbol{U} = \boldsymbol{Gm} \quad (1)$$

where $\boldsymbol{U}$ is the ground displacement vector at the receiver; $\boldsymbol{G}$ is the spatial derivative of Green's function, which contains the propagation effects between the source and receiver; and $\boldsymbol{m}$ terms are composed of the nine moment tensor components of the point source. We often assume that the event

is a point source parameterized by a centroid moment tensor, where the primary parameters are the moment tensor, centroid location, and time. Bayesian inversion framework offers a powerful approach for parameter estimation, integrating prior knowledge, effectively handles uncertainty, and provides robust, and interpretable results. It consists of three parts: (1) transforming prior information into prior distributions, (2) calculating the posterior probability and storing sufficient samples, and (3) statistics and analysis of model parameters (Vasyura-Bathke et al., 2021). The posterior probability distribution of the model parameters is the key to Bayesian inversion and can be written as follows:

$$p\left(m|d_{\text{obs}}\right) \propto p(m)\, p\left(d_{\text{obs}}|m\right) \tag{2}$$

where m mainly includes the source and hierarchical parameters (hyper-parameters), and d_{obs} is the displacement waveform data monitored by the geophone. The likelihood function is defined as

$$\rho_{\text{D}}(d) = \left[(2\pi)^{N} \det \boldsymbol{C}_{d}\right]^{-1/2} \exp\left[-\frac{1}{2}(d-d_{\text{obs}})^{\text{t}}\, \boldsymbol{C}_{d}^{-1}(d-d_{\text{obs}})\right] \tag{3}$$

where N is the number of valid waveforms; $\boldsymbol{C}_d$ is the covariance matrix (uncertainty function) of the displacement data d. $(d-d_{\text{obs}})^{\text{t}}\, \boldsymbol{C}_{d}^{-1}(d-d_{\text{obs}})$ measures how the observed data deviates from the model prediction. To monitor the potential instability of the fault system, a 16-channel seismological observation system with 32 geophones was installed in the Dongtan coal mine. The frequency range of the geophones was 1–600 Hz, the sampling rate was 500 Hz, the vertical resolution of the A/D converter was 16 bits, and the maximum data transfer rate was 1 MB/s. We used the criteria reported by Si et al. (2020) to convert between energy and M_{L} for high-energy seismic events ($M_{\text{L}} \geq 0.754$) as follows:

$$\log_{10} E = 1.9 M_{\text{L}} + 1.8 \tag{4}$$

Previous research has emohasized the crucial need of a three-dimensional velocity model to enhance the accuracy of inversion results (Heimann et al., 2019). We utilized various parameters, including density, thickness, wave velocity, as well as measured logging and geological data to establish a Type-B Green's function (Vasyura-Bathke et al., 2020). This inversion process was performed using the *beat* Bayesian inversion framework. Sampling was performed using Metropolis Hastings sampling (MHS) (Yildirim, 2012), with a total of 7500 chains across 15 stages used in each routine.

3.2. Numerical approach

3.2.1. Fracture modes used in the numerical approach

We analyze mining-induced tremors through two types of shear fracture models: in-plane and out-of-plane. The kinematics of earthquake rupture is described by the dislocation of two fault planes, described by their strike and dip, relative to each other. In dislocation theory, a shear rupture is represented as a pair of shear forces that are momentum-free in the sum. Typical examples of shear fracture modes are commonly found in overlying strata and in the fault slip regions due to mining operations. Mode II corresponds to an in-plane strike-slip shear rupture that propagates parallel to the direction of fault slip, whereas Mode III involves fracture propagation perpendicular to the fault slip direction.

3.2.2. Friction laws used in the numerical approach

Fracture nucleation, growth, and termination of faults are significantly influenced by constitutive frictional behavior. Slip weakening (SW) and rate state (RS) friction laws are selected to capture the dynamic and static behaviors of faults under mining-induced stresses. These laws have been broadly applied (Bizzarri and Cocco, 2003; Rojas et al., 2009) in many aspects, offering confidence in their applicability for accurately simulating fault behavior in mining environments.

(1) Slip-weakening friction law (Andrews, 1985)

Previous rock physics experiments have demonstrated that the friction coefficient decreases as the fault slip rate increases. Based on this premise, an SW friction criterion is proposed:

$$T = \begin{cases} \left[\mu_{\text{f}} + (\mu_{\text{s}} - \mu_{\text{f}})\dfrac{V_0}{V}\right]\sigma_{\text{n}} & (V \geq V_0) \\ \mu_{\text{s}}\sigma_n & (V < V_0) \end{cases} \tag{5}$$

where V_0 represents the reference slipping rate. The static friction coefficient μ_{s} quickly decreases to the dynamic friction coefficient μ_{f} when the slip rate V gradually increases beyond V_0. As V decreases, the friction coefficient gradually increases, forcing the rupture to gradually arrest. This law can represent self-healing on faults and has been implemented in the numerical model used in this study.

(2) Rate-and-state friction law (Fukuyama and Madariaga, 1998)

In this approach, we use the 'TPV102' benchmark problem for planar fault dynamics rupture (Harris et al., 2009; Duru, 2016). The application of the RS friction model is described briefly as follows, where the shear strength of the fault plane varies nonlinearly according to the friction law:

$$\tau = a\sigma_{\text{n}} \operatorname{arcsin} h\left\{\frac{V}{2V_0}\exp\left[\frac{f_0 + b\ln(V_0\psi / L)}{a}\right]\right\} \tag{6}$$

where $\mathrm{d}\psi/\mathrm{d}t = 1 - V\psi/L$ and couples with the state evolution equation defined by the aging law. The reference slip rate is denoted as V_0, and f_0 is the friction coefficient under the reference slip velocity. The parameter a is the direct effect used to describe the response of the model under changes in velocity and b is the evolution effect used to describe changes in steady-state friction with L being a critical slip distance. To contain the fault rupture, the velocity weakening law is applied inside the fault footprint, while velocity strengthening is applied outside the fault area (Fig. 2). Consequently, the fault is more likely to fracture and expand in the inner region, where the friction coefficient decreases with slip velocity. Outside this region, however, the friction coefficient increases with slip velocity, preventing further fault propagation. The transition from velocity weakening to velocity strengthening is achieved by increasing a (x, y) with a transition layer (width w = 0.1 km).

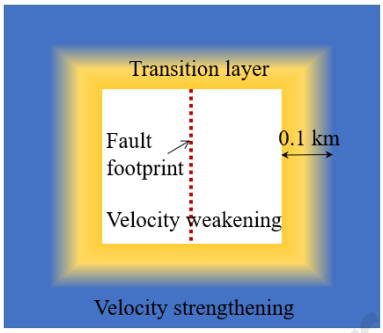

Fig. 2. Schematic diagram of numerical fault model. Velocity weakening is applied inside the fault area (white color), and velocity strengthening outside the fault area (blue color). A transition layer (yellow color) allows to adapt fraction laws.

We have $\Delta a(x, y) = 0.008\{1 - B(x - x_0; W/2, W)\,B(y; W; w)\}$, where

$$B(y;W;w) = \begin{cases} 1 & (|y| \le W) \\ \dfrac{1}{2}\left\{1 + \tanh\left[\dfrac{w}{|y| - (W+w)} + \dfrac{w}{|y| - W}\right]\right\} & (W \le |y| \le W + w) \\ 0 & (|y| \ge W + w) \end{cases} \tag{7}$$

Function $B(y; W; w)$ is the boxcar function. In case of mode II fracture, the initial two-dimensional stress tensor applied to the fault is $\sigma^0 = \begin{pmatrix} \sigma^0_{xx} & \sigma^0_{xy} \\ \sigma^0_{yx} & \sigma^0_{yy} \end{pmatrix}$, with the traction force acting on the fault calculated as $T^0 = \begin{pmatrix} T^0_x \\ T^0_y \end{pmatrix} = \sigma^0 \boldsymbol{n}$, $\begin{pmatrix} T^0_n \\ T^0_m \end{pmatrix} = \boldsymbol{R}T^0$, where $\boldsymbol{R}$ is the unit rotation matrix, and $\boldsymbol{n}$ is the normal vector. The normal vector $\boldsymbol{n} = (1, 0)^T$ and rotation matrix $\boldsymbol{R}$ are both identity matrices because the unit vector on the fault plane is a canonical basis vector. At time $t = 0$, the onset of horizontal fault slip occurs with initial velocity $V = V_{\mathrm{ini}}$, and is subjected to initial shear force and normal stresses of $\tau = T^0_m$ and $\sigma_{\mathrm{ini}} = -T^0_n$, respectively. The initial state variable is $\psi_{\mathrm{ini}}(x, y)$ (see Eq. (8)). The initial velocity and stress remain constant, while the initial state variable changes over time.

$$\psi_{\mathrm{ini}}(x,y) = \frac{L}{V_0}\exp\left\{\frac{a(x,y)\ln\left\{2\sinh\left[\tau_{\mathrm{ini}}/a(x,y)\sigma_{\mathrm{ini}}\right]\right\} - f_0 - a(x,y)\ln(V_{\mathrm{ini}}/V_0)}{b}\right\} \tag{8}$$

Applying horizontal shear traction disturbance from t = 0 causes the fault to rupture and nucleate as follows (Duru et al. 2016):

$$\left.\begin{aligned} \Delta\tau(x,y,t) &= \Delta\tau_0 F(r) G(t) \\ r &= \sqrt{(x - x_0)^2 + (y - y_0)^2} \end{aligned}\right\} \tag{9}$$

where r is the radius of the finite region of the fault, and

$$F(r) = \begin{cases} \exp\left(\dfrac{r^2}{r^2 - R^2}\right) & (r < R) \\ 0 & (r \ge R) \end{cases} \tag{10}$$

$$G(t) = \begin{cases} \exp\left[\dfrac{(t-T)^2}{t(t-2T)}\right] & (0 < t < T) \\ 1 & (t \ge T) \end{cases} \tag{11}$$

During the period $0 < t < T$, the shear traction force gradually increases from 0 to $\Delta\tau$ within the radius of R.

3.2.3. Numerical model setup

The numerical discretization method known as SBP-SAT is widely used in finite difference and finite element methods, which is crucial for

capturing complex dynamics like fault slip. However, it requires computationally intensive computations and careful handling of boundary conditions to ensure stability and accuracy. The primary concept involves dividing the solution domain into smaller modules. Within the computational domain, the SBP-SAT method has a significant advantage in handling predefined crack paths, allowing for more accurately simulation of the full fault slip process (Abgrall et al., 2020; Eriksson, 2021). Additionally, the finite-difference technique developed using this method has enhanced the accuracy and the stability of model results.

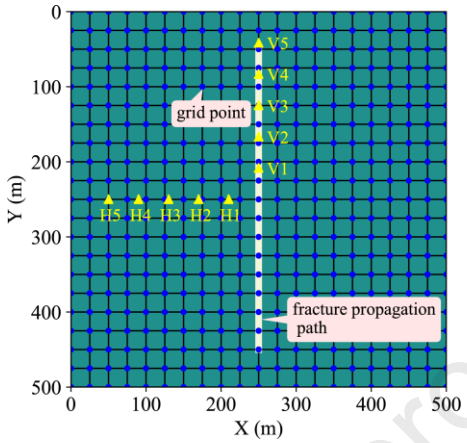

Fig. 3. Discretization model. Nodes and computational grids are represented by blue circles and black lines, respectively. The P-wave velocity parameter used in this model is 4.2 km/s. The fracture propagation path is indicated by the white dashed line.

We performed a dynamic slip simulation to represent the nucleation of a pure shear source, fracture propagation, and arrest. The simulation considered two shear rupture modes and two friction laws. A discretization model was established to evaluate stress variations during fault slip, as shown in Fig. 3. The fault rupture is 500 m long (indicated by the white dashed line in Fig. 3), consistent with the observed size of medium-sized faults in the coal mine. Five monitoring locations were set up horizontally (H1-H5) and vertically (V1-V5) to record stress changes during the fault slip process. Normal and shear loads of 25 MPa and 45 MPa, respectively, were applied to the fault. We used a traction vector to initiate fault slip, similar to that used for mining-induced fault slip. The shear slip simulation process involves several steps: (1) establishing a discretization model and setting monitoring points, (2) selecting the shear fracture mode and friction law, (3) assigning model parameters and friction law parameters, and (4) interactive plotting and data export after model run. Table 1 lists the specific model parameters that were applied. To systematically study fault slip, the following four scenarios were modeled: (a) Mode II fracture with RS friction law (RS–II); (b) Mode III fracture with RS friction law (RS–III); (c) Mode II fracture with SW friction law (SW–II); and (d) Mode III fracture with SW friction law (SW–III).

Table 1. Simulated model parameters of fault slip with rate and state friction law and slip weakening law.

Scenario	Parameter	Value
Basic properties of the model	Length (km)	0.25
	Width (km)	0.5
	Grid points in *X*-axis	20
	S-wave velocity (km/s)	2.43
	Density (kg/m^3)	2.5
	Spatial order of accuracy	4
	Grid points in *Y*-axis	40
	Snapshot frequency (s)	0.01
	P-wave velocity (km/s)	4.2
	σ_{xx}	0
	σ_{yy}	0
	σ_{yx}	$-1/\sqrt{2}$
	σ_{xy}	$-1/\sqrt{2}$

SW-II and SW-III	τ_{ini} (MPa)	25
	Dynamic friction coefficient	0.42
	σ_{ini} (MPa)	45
	Critical slip	0.005
	Static friction coefficient	0.59
	Total duration (s)	0.04
RS-II and RS-III	a	0.008
	Reference friction coefficient	0.6
	τ_{ini} (MPa)	25
	b	0.01
	L	0.0011
	σ_{ini} (MPa)	45
	V_0 (km/s)	1×10^{-25}
	V_{ini} (km/s)	2×10^{-12}
	Total duration (s)	0.24

4. Field results

4.1. Mechanism of mining-induced tremors induced by FQ14 fault slip

Particularly, the FQ23, 3FQ80, FQ12, FQ13 and FQ14 faults have strikes approximately perpendicular to the working face. The abutment pressure from the advancing working face is superimposed on the background stress field of the fault, causing localized stress concentration. Therefore, there is a possibility of local instability due to stress concentration at the tip of the FQ14 fault, which has also triggered a series of MS events. Therefore, the slip of the FQ14 can be easily induced. Given the current mining position shown in Fig. 4, stability monitoring of the FQ14 fault will be the focus of future work.

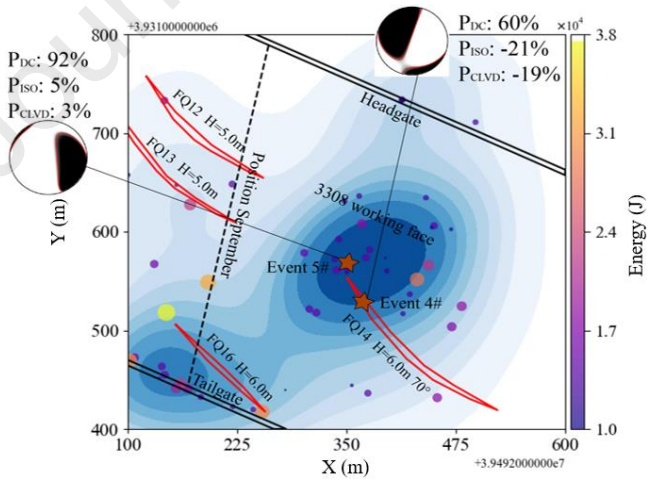

Fig. 4. Distribution and inversion of MS sources surrounding the FQ14 fault (circle dots). The diagram includes two black lines at top and bottom representing headgate and tailgate, respectively. Blue contour lines illustrate the density of events, and the dashed line represents the current mining position of the working face. This area includes four faults: FQ12, FQ13, FQ14 and FQ16.

As illustrated in Fig. 1, seven MS events associated with nearby faults were inverted for MT. According to the results of moment tensor decomposition, the dominant factor restricting safety mining is the shear-type source. Considering the spatiotemporal distribution of these sources, events #4 and #5 were particular influential in triggering subsequent events within the fault region. They were mainly distributed at the tip of the fault with shear rupture, likely due to elevated abutment pressure and fault stress field within the fault region. As shown in Fig. 4, these events may have created conditions leading to the overall instability of the FQ14 fault. Thus, we focus is on understanding the occurrence mechanisms of events #4 and

#5, which are crucial for the planning the upcoming stages of mining that will interest with the FQ14 fault.

4.2. Displacement fields after FQ14 fault slip

Events #4 and #5 occurred on 23 and 24 August 2022, respectively (Table 2). No further MS events were reported within the detection limit following event #4. As shown in Fig. 5, we analyzed slip vectors using MT results of events #4 and #5 to explore the relationship between mining-induced tremors caused by faults and subsequent events (Toda et al., 2011).

Table 2. Inversion results of high-energy MS hypocenters surrounding the faults.

No.	FMT	Date	Time (s)	Strike 1 (°)	Dip 1 (°)	Rake 1 (°)	Strike 2 (°)	Dip 2 (°)	Rake 2 (°)	Magnitude	Misfit	Type of rupture
#1		2022-05-01	2:26:00	88	89	-90	276	1	-83	1.25	0.12	S
#2		2022-08-22	9:17:10	82	65	-7	176	83	-155	1.35	0.09	S
#3		2022-08-23	9:04:20	140	89	-84	241	6	-169	1.07	0.11	S
#4		2022-08-23	2:56:22	104	28	-5	199	88	-118	1.18	0.2	S
#5		2022-08-24	2:58:56	242	19	-24	355	82	-107	1.33	0.05	S-C
#6		2022-12-10	3:03:41	304	73	-172	211	82	-17	1.04	0.14	S-T
#7		2022-12-20	8:51:23	73	85	91	246	5	84	1.07	0.17	S

Note: C = Compression, T = Tensile, S = Shear.

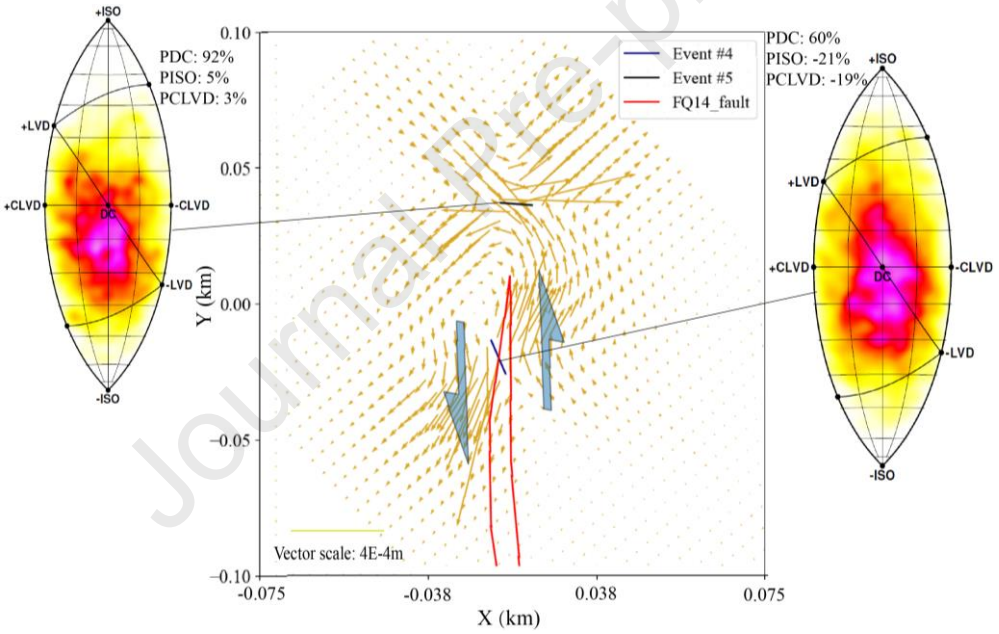

Fig. 5. The distribution of the displacement field (olive green arrows) is illustrated by olive green arrows, focusing on two high-energy tremors (marked #4 and #5). Arrows represent the direction of displacement, and their length representing the magnitude. The larger green arrow denotes the movement direction of the fault FQ14 under consideration. The probability distribution of events #4 and #5 is depicted in lune clouds on both sides of the diagram, with red indicating an increasing likelihood of occurrence. Compared to Figs. 1 and 4, this figure has been rotated for better alignment with the simulations in the following chapters.

According to the spatiotemporal distribution of sources in Fig. 4, event #5 was induced by the preceding event #4, primarily because event #5 occurred at the fault tip, an area with intense stress concentration. The lune-type plot in Fig. 5 shows that the main cause of these two events was shear rupture, followed by many low-energy events. From the displacement vectors of events #4 and #5 in Fig. 5, it is observed that the direction of the displacement vectors aligns with the fault strike. This suggests a potential trend of instability near the southeast end of the fault. Field observations indicate that the 3307 goaf shed significant lateral support pressure on the working face during the mining operation. This likely influenced the rupture direction of seismic event #5 (strike, dip and rake are 242°, 19° and 24°, respectively). Additionally, event #4 is more likely to have slipped along the existing plane of weakness, i.e. the FQ14 fault. The following section will discuss the stress-dependent spatiotemporal relationships between the selected MS events of interest (refer to Table 2 for high-energy seismic events).

5. Model results: The effect of predicting the rupture of FQ14 fault

Field studies indicate that high-energy events in fault area exhibit a high double-couple component. To simplify our model, we establish a pure shear model to study the evolution of relevant properties following the slip of the FQ14 fault. Due to the complexities of underground engineering, obtaining precise properties of fault planes is challenging. Therefore, we introduce different friction criteria to examine the characteristics of fault slip (Orlecka-Sikora et al., 2009). Based on this approach, we conducted a forward simulation to investigate the dynamic rupture process of the shear source using two friction laws.

5.1. Dynamic rupture process of shear source under different friction laws

5.1.1. Shear stress

For mode II, there are two regions with opposite shear stress directions on one side of the fault (areas A and B), as depicted in Fig. 6a and c. The modeled shear stress distribution aligns with the moment tensor composition results observed for event #5 (see Fig. 5). In contrast, this phenomenon does not exist in the mode III fracture source scenarios. In this scenario, the range of influence of the shear stress caused by fault rupture was much smaller compared to mode II fracture scenario. Furthermore, the range of stress influence under the SW friction law is significantly smaller than that the RS friction model. There is a significant increase in shear stress at the fault tip under the RS friction law. Based on these model results, the RS friction model provides a better agreement with the observed data from MTI in the previous section.

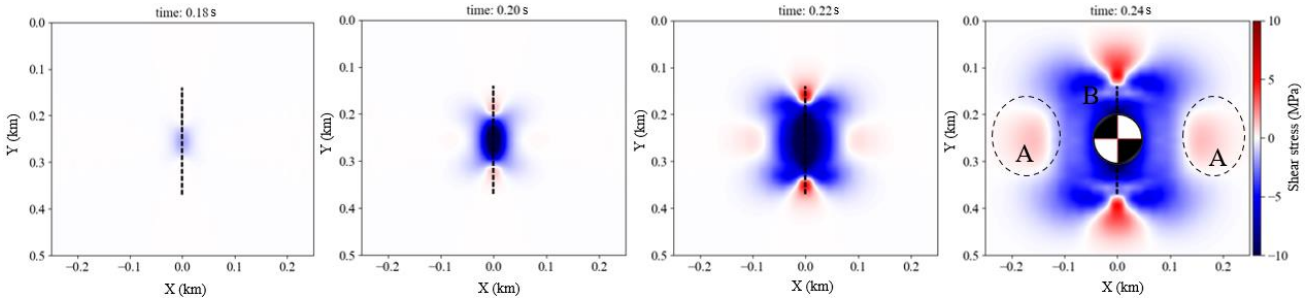

(a) Model scenario RS-II.

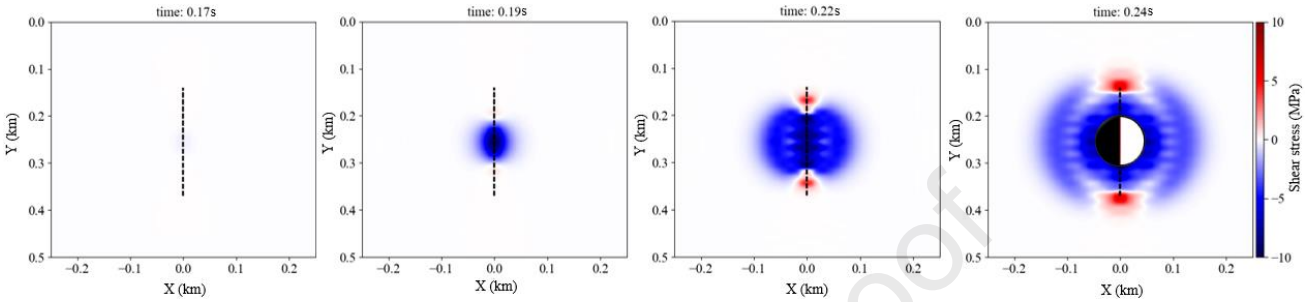

(b) Model scenario RS-III.

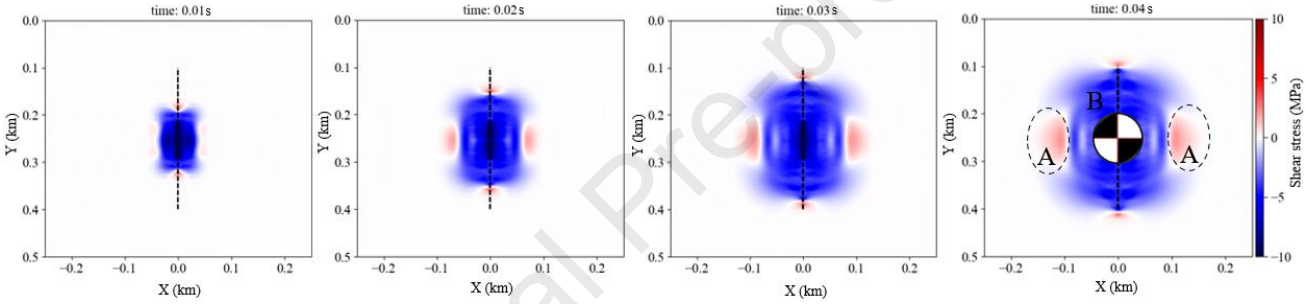

(c) Model scenario SW-II.

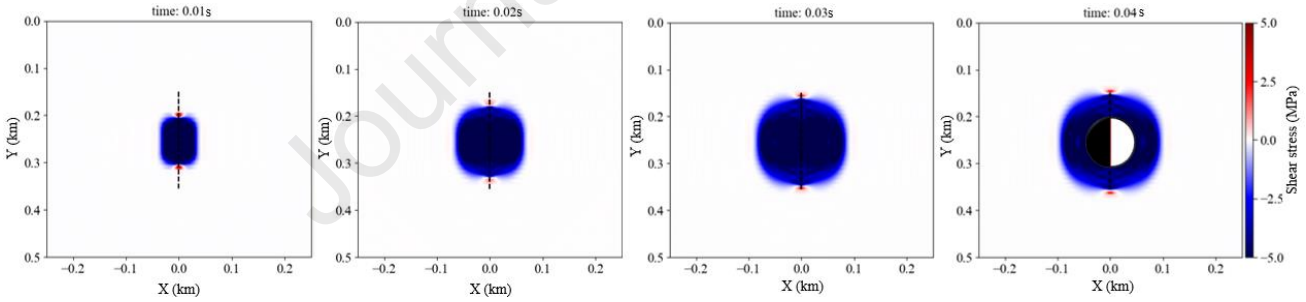

(d) Model scenario SW-III.

Fig. 6. Evolution of shear stresses in four model fault scenarios: (a) Rate and state model with in-plane shear rupture source, (b) Rate and state model with out-of-plane shear rupture source, (c) Slip weakening model with in-plane shear rupture source, and (d) Slip weakening model with out-of-plane shear rupture source. The direction of the fault is consistent with the orientation in Fig. 5.

5.1.2. Normal stress

Fig. 7 shows the evolution characteristics of normal stress for different model scenarios. It is interesting to note that the RS friction law results in a wider normal stress influence range compared to the SW friction law, which is consistent with the observed pattern of shear stress variation. The crack tip of the fault is the position of the normal stress concentration, and as the crack tip moves, the stress concentration gradually migrates upwards while the stress magnitude at the initial position gradually decreases. The overall changes in normal stress exhibit a pattern of decreasing, then increasing, and finally decreasing again as the distance increases from both sides of the fault. This also explains why the events in Fig. 6 were mostly located within a certain distance from the fault.

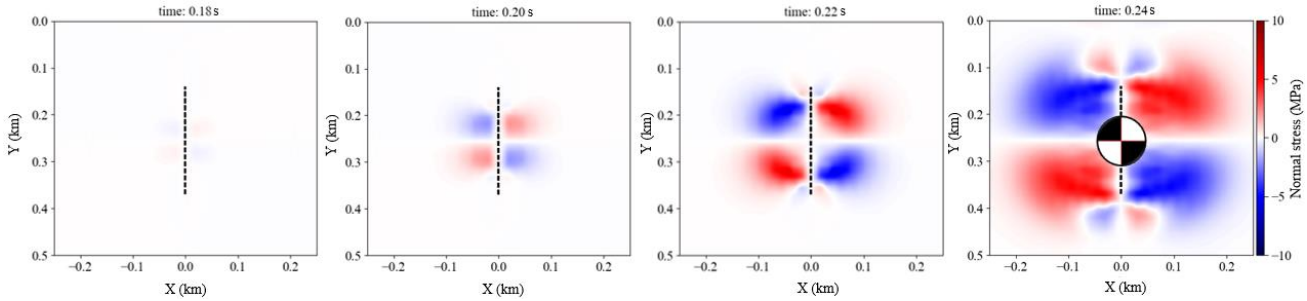

(a) Model scenario RS-II.

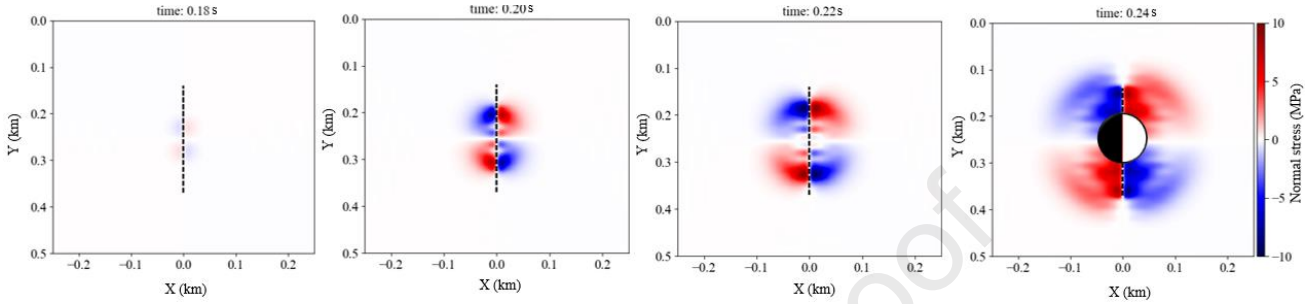

(b) Model scenario RS-III.

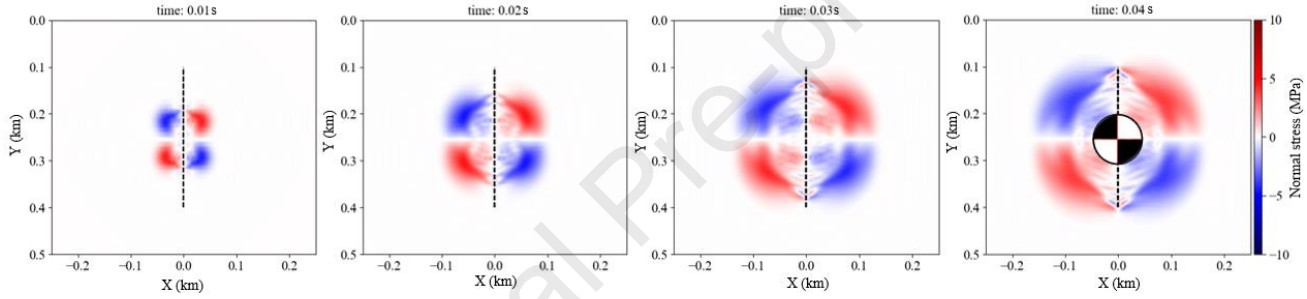

(c) Model scenario SW-II.

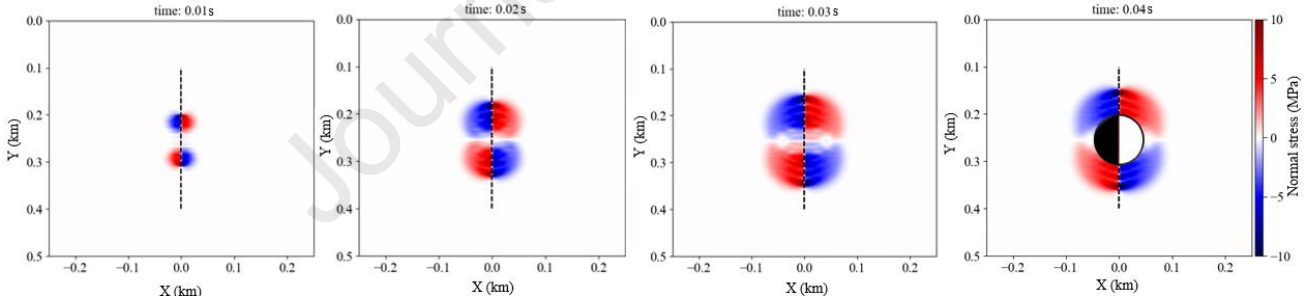

(d) Model scenario SW-III.

Fig. 7. Evolution of normal stresses for the four modeled fault scenarios: (a) Rate and state model with in-plane shear rupture source, (b) Rate and state model with out-of-plane shear rupture model, (c) Slip weakening model with in-plane shear rupture source, and (d) Slip weakening model with out-of-plane shear rupture source. The direction of the fault is consistent with the orientation in Fig. 5.

5.2. Parametric changes in fault plane during rupture process

5.2.1. Traction of fault plane

The traction variables can be used to evaluate the applicability of different friction laws to fault slip and reveal their dynamic behavior (Fig. 8). In both friction law scenarios, there is an accumulation of traction prior to the fault slip. The fault rupture process is fast in the RS mode; therefore, more energy is released during seismic monitoring (with a higher waveform amplitude) compared to other models. In the RS-III model, faults exhibit extremely unstable slip, which can easily induce multi-peak waveforms under field conditions. Under the same stress conditions, the size of the fault rupture in the SW-II model is relatively large. Based on these characteristics, the SW-II model can be used as an indicator to infer the mode of fault slip instability in the field.

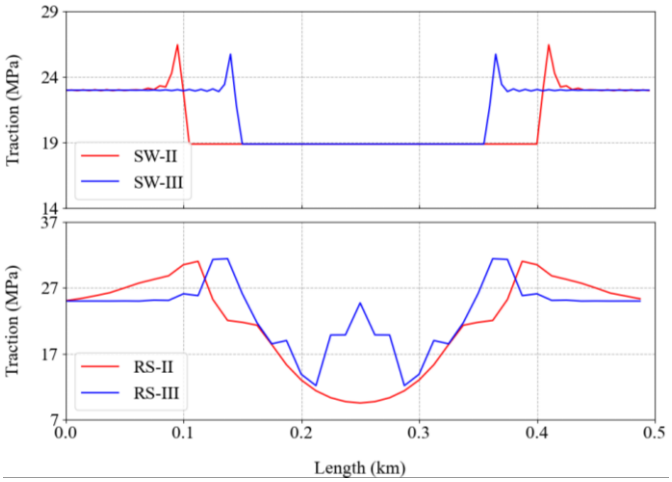

Fig. 8. Variations in traction along the fault plane during rupture of the fault in four different model scenarios: Slip weakening models (upper) and rate and state models (lower).

5.2.2. Slip rate

Fig. 9 depicts the slip rate of the fault evolution over time at different stages. As time progresses, the slip rate at the tail of the fault plane remains relatively high, whereas that inside the fault decreases steadily. The length of the fracture produced by the mode II rupture is longer than that of mode III at the same time. The RS friction law initiates static stress accumulation in the fault during the initial phase (0-0.17 s), followed by a rapid transition to slip instability at t = 0.17 s. This process of fault instability unfolds quickly, leading to an instantaneous release of energy and the generation of powerful seismic waves that significantly affect the stability of roadways in the mines. In mode II, the fault rupture plane extends horizontally in an elliptical shape, whereas in mode III, it also elongates vertically. This shape facilitates the concentration of shear stress on the fault, leading to a higher likelihood of unstable fracture propagation. Therefore, the fault slip process in mode III is more unstable compared to mode II.

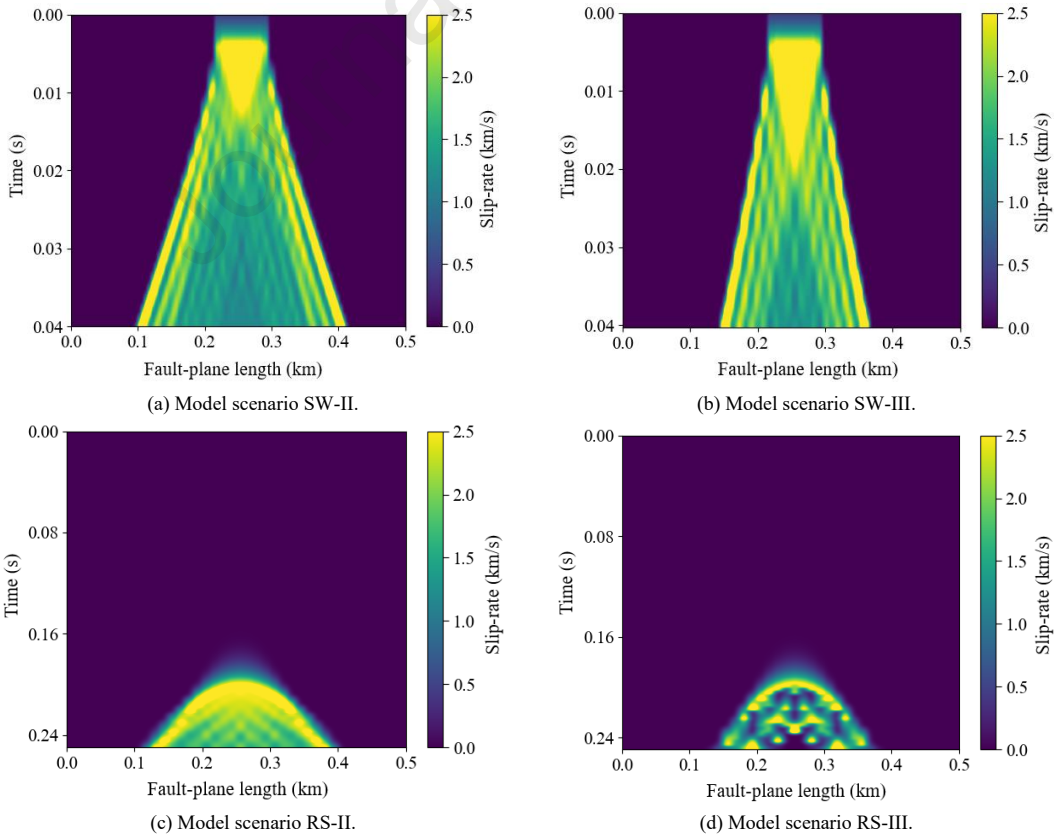

(a) Model scenario SW-II. (b) Model scenario SW-III.

(c) Model scenario RS-II. (d) Model scenario RS-III.

Fig. 9. Evolution of slip rate during dynamic rupture of the fault: (a) Slip weakening model with in-plane plane shear rupture source, (b) Slip weakening model with out-of-plane shear rupture source, (c) Rate and state model with in-plane shear rupture source, and (d) Rate and state model with

out-of-plane shear rupture model.

5.2.3. Stress changes at monitoring points

The shear stress variations at monitoring locations during fault slip under different schemes are illustrated in Fig. 10. During fault rupture, the RS friction law exhibits a higher peak stress and a longer duration of static stress compared to the SW. This prolonged static stress accumulation signifies increased energy build-up within the fault, leading to rapid rupture and the release of an intense stress wave. Monitoring points detect a sudden change in stress along the fracture, indicating stress redistribution within the fault region accompanied by a shift in shear stress direction. In the horizontal direction, the stress initially increases gradually; subsequently, oscillating fluctuations occur at a certain stress level (Fig. 10b and c), indicating the complex nature of the stress changes. The stress changes observed in the horizontal direction lacked regularity compared to those in the vertical direction.

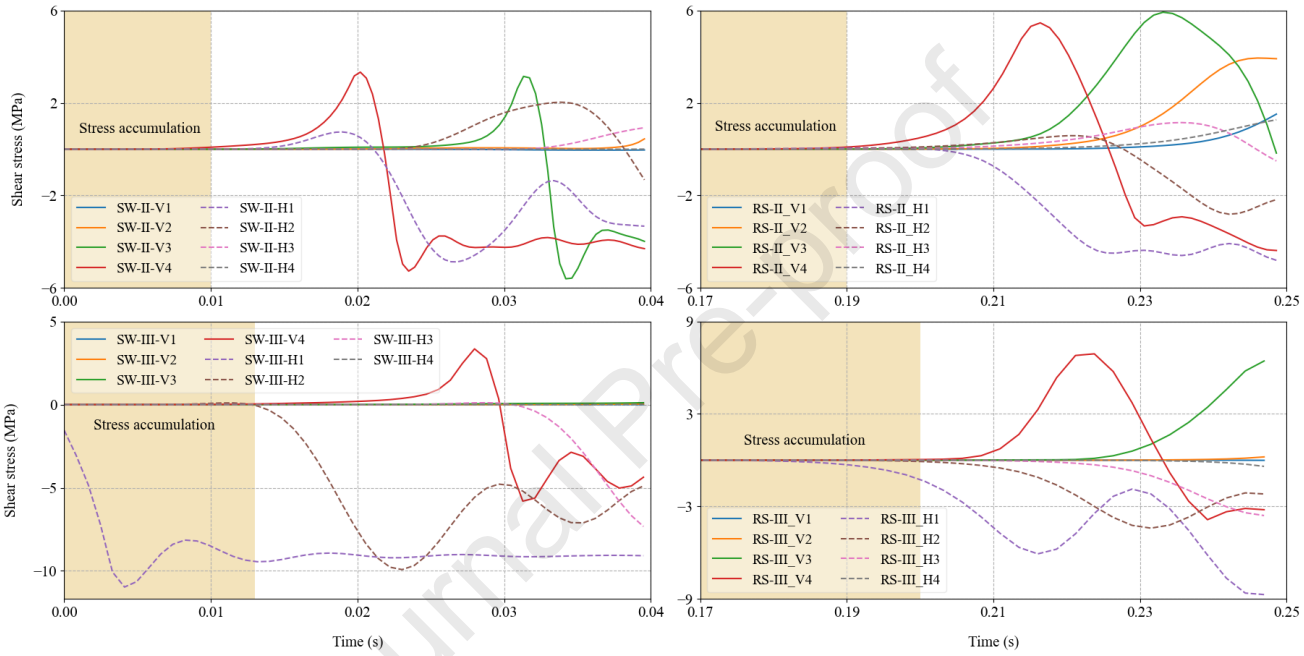

Fig. 10. Stress changes at monitoring locations during dynamic rupture for different model scenarios: (a) Slip weakening model with in-plane shear rupture source, (b) Rate and state model with in-plane shear rupture source, (c) Slip weakening model with out-of-plane shear rupture source, and (d) Rate and state model with out-of-plane shear rupture model. The locations of monitoring locations are shown in Fig. 7, where *V* and *H* represent the vertical and horizontal monitoring points, respectively.

6. Discussion

Numerous high-energy events have occurred in the 3308 working face, triggered by tectonic stresses modified by mining operations. We explore potential failure modes associated with the FQ14 fault and its subsequent phases. We analyse rupture mechanisms of events near the fault, followed by the construction of a forward model to discern the potential slip mode on FQ14.

6.1. Combined interpretation of field and rupture model results

The research findings reveal that shear rupture sources are prevalent near the fault zone. In nonlinear fracture mechanics, the stress singularity at the crack tip is replaced by a process zone. In Fig. 5, we observe that the displacement field and energy release rate associated with a shear fracture tip at the mine scale. Frozen-in shear fracture tips are challenging to replicate in laboratory tests (e.g. Zang et al. 2000). The elevated abutment pressure significantly raises the likelihood of fault activation and failure in this region, particularly under the influence of thick and hard rock stratum.

From Fig. 4, it is observed that the angle between the mining position and the fault is approximately 60°. Therefore, the orientation of the fault is not the most favourable for slip induced by mining-induced stress. However, as one end of the fault is close to the location of excavation and related stress transfer, it experiences local instability first (events #4 and #5). Subsequently, many events are primarily distributed within the disturbed area affected by these two events. As excavation continues, the portion of the fault under critical stress expands, and new events occur in accordance with

this migration pattern.

According to Fig. 11, event #5 exhibited a pattern consistent with the simulated distribution of shear stress after FQ14 fault slip. Outside the region of reduced shear stress on the fault plane, there is an area of increased stress, which is prone to triggering MS events. The simulated results align with the field observations in terms of these stress patterns. Following event #5, a series of MS events occurred, particularly in the region where shear stress is positively increased, as shown in Fig. 11. Additionally, the interaction between MS events and mining disturbances further induces fault slippage. This fault slippage, in turn, induces additional MS events. Besides, micro-fracturing is promoted by increases in shear stress while being restrained by decreases in shear stress. This complex interplay highlights how stress variations and mining operations can dynamically influence fault behaviour and seismicity in the study area. The mechanism of event #5 can be validated using the RS-II model scenario shown in Fig. 9a. Events #4 and #5 are identified as belonging to fracture mode-II based on the results of the MTI. This rupture mode has a larger stress influence range than the SW friction model, resulting in numerous aftershocks (Fig. 6). The extensive distribution of these aftershocks strongly suggests their association with the RS-II model. Events #4 and #5 played a significant role in promoting slip instability along the FQ14 fault, which is identified as mode-II rupture based on the displacement field presented in Fig. 5. Thus, we consider timely MTI and stress inversion analysis of MS sources near the fault zone crucial for assessing fault stability. Importantly, as depicted in Fig. A1 (Appendix A), fault rupture (assuming RS friction) occurs abruptly and is unstable even under low-stress conditions. This scenario poses a higher hazard compared to others and can significantly impact roadway safety.

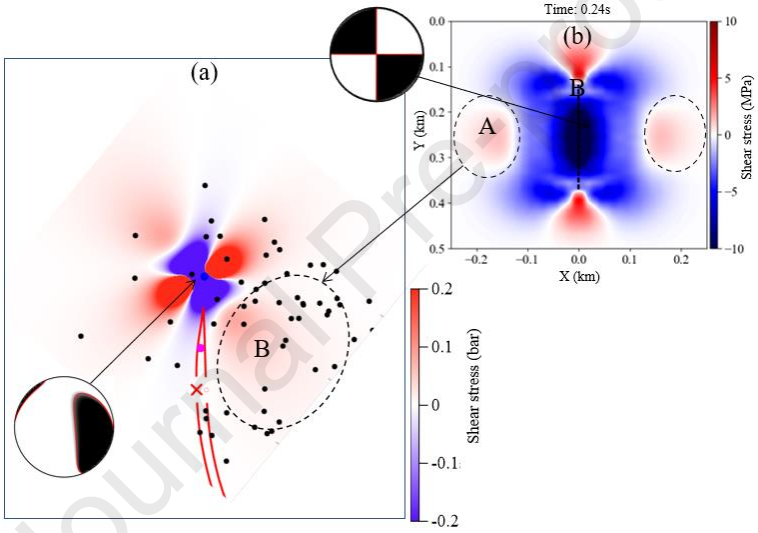

Fig. 11. Results of shear stress distribution for event #5 (data from the result of MT inversion) and fault slip (simulation): (a) The distribution of shear stresses caused by event #5. The locations of aftershocks following events #4 and #5 are indicated by black dots within the time window from 23 August 2022 to 29 September 2022. (b) Evolution of shear stresses in the rate and state model with an in-plane shear rupture source.

Incorporating observed moment tensors into forward modeling can help determine the potential increase in shear stress range. However, it is crucial to recognize that the range derived from these models may not perfectly match on-site conditions. Coal mine sites, unlike isotropic media assumed in inversion models, exhibit non-isotropic characteristics. Consequently, analyzing the stress tensors obtained from stress inversion enables a more precise understanding of fault stress perturbations. Consequently, analyzing the stress tensors obtained from stress inversion enables a more precise understanding of fault stress perturbations.

6.2. Application: Blasting for stress-relief to prevent fault slip and rockburst

Here, we present a case study from the Xinjulong coal mine, where insights from this study were applied to mitigate future dynamic disasters arising from fault instability. Combined with source parameters and Coulomb stress analysis, critical fault zones prone to slip can be identified (as discussed earlier), prompting the implementation of stress-relief measures. This included targeted blasting near the fault zone, as illustrated in Fig. 12. This approach has proven successful and validated for its effectiveness in preventing high-energy tremors. The selected 8302 working face is located in district No. 8 of the Xinjulong coal mine (Fig. 12). Fig. 12 shows the Huangtang syncline located in the east, the 8301 goaf (2019) located in the west, and the F21 and Bihai faults located in the northwest. The mining seam at Xinjulong coal mine ranges in depth from 906.5 m to 992.6 m, with an average thickness of 8.97 m. Overlying this seam are thick and hard interbeds consisting of medium sandstone, fine sandstone, and siltstone. Within the working face, the FG1 fault and several minor faults have been encountered, presenting potential instability concerns.

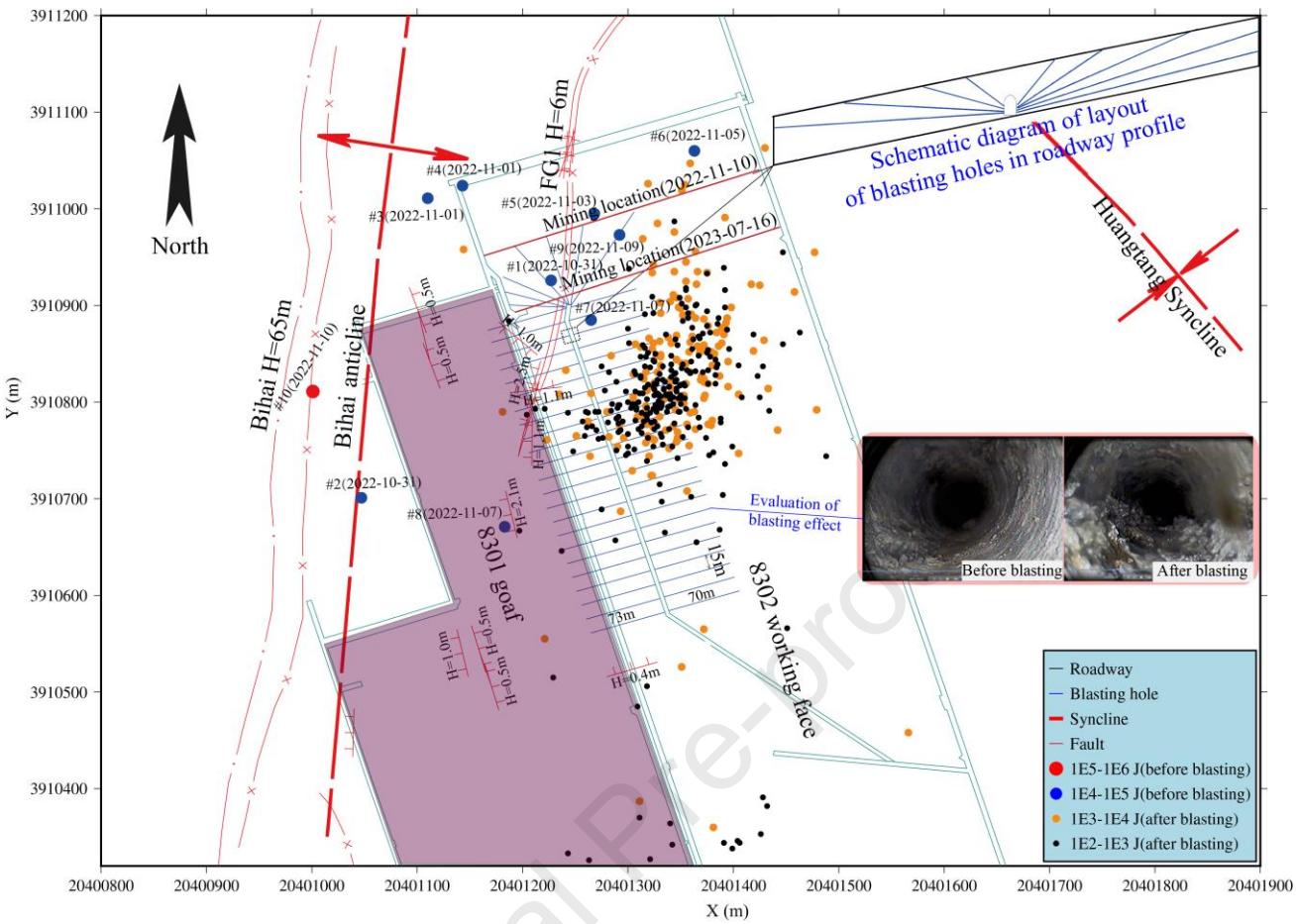

Fig. 12. Location of high-energy mining-induced tremors and layout of the 8302 working face roadways for the Xinjulong coal mine. The blasting borehole layout in the roadway is shown in the upper-right inset, and the middle-right inset depicts the state of boreholes before and after blasting. Prior to blasting, 10 high-energy MS events were recorded (blue dots). In the subsequent mining operations after blasting, the induced events exhibited energy ranging from 1×10^2 J to 1×10^4 J, represented by orange and black dots (events occurred from 16 July 2023 to 1 August 2023).

A total of 11 high-energy MS events occurred in the 8302 working face from 13 October 2022 (start mining) to 10 November 2022. Most of them (events # 1, # 5, # 7, # 8, #9 and #10) clustered in the vicinity of the FQ1 fault zone (Fig. 12), especially event #8 occurred at the tip of the fault (consistent with the mechanism of event #5 in Fig. 5). To mitigate rockburst accidents stemming from fault instability, management decided to stop mining operations and implemented blasting pressure-relief measures. The primary objective of these measures was to alleviate stress concentrations near the FG1 fault zone and reduce elevated abutment pressure. Analysis of the data from 16 July 2023 to 1 August 2023 indicates a decrease in the energy of events following the blasting. The energy levels ranged mainly between 1×10^2 J and 1×10^4 J (Fig. 12). This outcome suggests that the implementation of blasting pressure-relief measures targeting the fault and roof effectively decreased the likelihood of high-energy events occurring in this region.

7. Conclusions

This study uses Bayesian MTI and SBP-SAT forward simulations to identify the source mechanisms of mining-induced seismicity for the mapped FQ14 fault. The main results of this study are summarized below:

(1) Bayesian moment tensor reveals shear as the dominant rupture type for mining-induced high-energy events near mapped faults in Carboniferous strata at the Dongtan coal mine in China. The clustering of these events near the fault is associated with elevated abutment pressures and fault tectonic stress, and in combination with displacement fields provided insights into frozen-in tip stresses at the mine scale.

(2) Stress increase areas/volumes at shear fracture tips are smaller in SW models with in-plane shear compared to RS models. Faults with an in-plane

strike-slip had longer rupture lengths than those with an out-of-plane slip. For the pure-shear source, distinct regions of increased and decreased shear stress were observed on either side of the fault plane, explaining why tremor hypocenters tend to occur at certain distances from faults.

(3) The RS friction law exhibited relatively high peak stress with a longer duration of static stress accumulation compared to slip weakening. This suggests that the rate-and-state model generates a rapid release of intense stress. Higher dynamic friction coefficients resulted in lower slip rates and shorter rupture lengths, and increased normal stress reduced fault rupture length. At low normal stress levels, significant instability in slip rates was observed at various fault segments under the RS model, characterized by multiple peaks in slip rates.

(4) Based on these results, we propose that MTI and modeling should be routinely used to identify potentially unstable fault zones. This is important even though the results obtained by modeling may not be consistent with the actual situation on site due to the impact of mining disturbance on the stress regime. Subsequently, by analyzing the stress tensor derived from the stress inversion, we can precisely determine the extent of stress perturbations caused by fault slip. This allows us to accurately identify areas of elevated shear stress and guide the implementation of stress-relief measures.

Data availability statement

Simulation code and on-site waveforms data can be downloaded from Zenodo (https://doi.org/10.5281/zenodo.8404703). The on-site data are sourced from the Seismological Observation System in the Dongtan coal mine, and the simulation code can be executed via the Jupyter-Notebook. Source code was developed by Daniel Koehn. Thank you for sharing the relevant materials and source code in GitHub (https://github.com/daniel-koehn), which provided valuable guidance for this work.

Declaration of competing interest

The authors declare that they have no known competing financial interests or personal relationships that could have appeared to influence the work reported in this paper.

Acknowledgments

We gratefully acknowledge the Graduate Innovation Program of China University of Mining and Technology, the Fundamental Research Funds for the Central Universities (Grant No. 2023WLKXJ017), the Postgraduate Research & Practice Innovation Program of Jiangsu Province (Grant No. KYCX23_2776), and the Shandong Energy Group (Grant No. SNKJ2022BJ03-R28). Derek Elsworth gratefully acknowledges support from the G. Albert Shoemaker endowment. Pictures were illustrated using Matplotlib, Generic Mapping Tools (GMT) version 6, and Pyrocko.

References

Abgrall, R., Nordström, J., Öffner, P., Tokareva, S., 2020. Analysis of the SBP-SAT stabilization for finite element methods. Part I: Linear Problems. J. Sci. Comput. 85(2), 1–29.

Andrews, D., 1985. Dynamic plane-strain shear rupture with a slip-weakening friction law calculated by a boundary integral method. Bull. Seismol. Soc. Am. 75(1), 1–21.

Bai, Q., Konietzky, H., Ding, Z., Cai, W., Zhang, C., 2021. A displacement-dependent moment tensor method for simulating fault-slip induced seismicity. Geomech. Geophys. Geo-energ. Geo-resour. 7, 1–25.

Bentz, S., Martínez-Garzón, P., Kwiatek, G., Bohnhoff, M., Renner, J., 2018. Sensitivity of full moment tensors to data preprocessing and inversion parameters: A case study from the Salton Sea Geothermal Field. Bull. Seismol. Soc. Am. 108(2), 588–603.

Bizzarri, A., Cocco, M., 2003. Slip-weakening behavior during the propagation of dynamic ruptures obeying rate- and state- dependent friction laws. J. Geophys. Res.: Solid Earth 108(B8), 2373.

Braunmiller, J., Nabelek, J., Ghods, A., 2020. Sensor orientation of Iranian broadband seismic stations from P-wave particle motion. Seismol. Res. Lett. 91(3), 1660–1671.

Cao, J., Dou, L., Konietzky, H., Zhou, K., Zhang, M., 2023. Failure mechanism and control of the coal bursts triggered by mining-induced seismicity: a

case study. Environ. Earth Sci. 82(7), 168.

Cesca, S., Buforn, E., Dahm, T., 2006. Amplitude spectra moment tensor inversion of shallow earthquakes in Spain. Geophys. J. Int. 166(2), 839–854.

Dang, P., Liu, Q., Song, J., 2020. Simulation of the Jiuzhaigou, China, earthquake by stochastic finite-fault method based on variable stress drop. Nat. Hazards 103(2), 2295–2321.

Deng, S., Li, J., Jiang, H., Wang, M., 2018. Experimental and theoretical study of the fault slip events of rock masses around underground tunnels induced by external disturbances, Eng. Geol. 233, 191–199.

Dou, L., Mu, Z., Li, Z., Cao, A., Gong, S., 2014. Research progress of monitoring, forecasting, and prevention of rockburst in underground coal mining in China. Int. J. Coal Sci. Technol. 1, 278–288.

Duan, Y., Si, G., Canbulat, I., Luo, X., 2022. Temporal-spatial characterization of mining-induced seismicity in the vicinity of a dyke – A case study. Eng. Geol. 307, 106788.

Dufumier, H., Rivera, L., 1997. On the resolution of the isotropic component in moment tensor inversion. Geophys. J. Int. 131(3), 595-606.

Duru, K., 2016. Dynamic earthquake rupture simulations on nonplanar faults embedded in 3d geometrically complex, heterogeneous elastic solids. J. Comput. Phys. 305, 185–207.

Eriksson, S., 2021. Inverses of SBP-SAT finite difference operators approximating the first and second derivative. J. Sci. Comput. 89(2), 30.

Feng, G., Feng, X., Chen, B., Xiao, Y., Yu, Y., 2015. A microseismic method for dynamic warning of rockburst development processes in tunnels. Rock Mech. Rock Eng. 48, 2061–2076.

Fukuyama, E., Madariaga, R., 1998. Rupture dynamics of a planar fault in a 3D elastic medium: rate-and slip-weakening friction. Bull. Seismol. Soc. Am. 88(1), 1–17.

Gao, F., Kang, H., Li, J., 2021. Numerical simulation of fault-slip rockbursts using the distinct element method. Tunn. Undergr. Space Technol. 110, 103805.

Guo, Y., Lu, C., He, Z., Song, J., 2022. Numerical and field investigations of tremors induced by thick-hard strata fracture. Appl. Sci. 12(21), 11151.

Hamidbeygi, M., Vasyura-Bathke, H., Dettmer, J., Eaton, D.W., Dosso, S.E., 2023. Bayesian estimation of nonlinear centroid moment tensors using multiple seismic data sets. Geophys. J. Int. 235(3), 2948–2961.

Harris, R.A., Barall, M., Archuleta, R., et al., 2009. The SCEC/USGS dynamic earthquake rupture code verification exercise. Seismol. Res. Lett. 80(1), 119–126.

He, S., Chen, T., Vennes, I., He, X., Song, D., Chen, J., Mitri, H., 2020. Dynamic modelling of seismic wave propagation due to a remote seismic source: A case study. Rock Mech. Rock Eng. 53, 5177–5201.

He, Z., Lu, C., Zhang, X., Guo, Y., Meng, Z., Xia, L., 2022. Numerical and field investigations of rockburst mechanisms triggered by thick-hard roof fracturing. Rock Mech. Rock Eng. 55(11), 6863–6886.

Heimann, S., Vasyura-Bathke, H., Sudhaus, H., et al., 2019. A Python framework for efficient use of pre-computed Green's functions in seismological and other physical forward and inverse source problems. Solid Earth 10, 1921–1935.

Hu, F., Huang, H., Chen, X., 2017. Effect of the time-weakening friction law during the nucleation process. Earthq. Sci. 30, 91–96.

Im, K., Avouac, J., 2022. Linear stability analysis of the condition for vibration during frictional slip. J. Mech. Phys. Solids 167, 104993.

Iwata, T., 2018. A Bayesian approach to estimating a spatial stress pattern from P wave first-motions. J. Geophys. Res.: Solid Earth 123(6), 4841–4858.

Jiang, L., Kong, P., Zhang, P., Shu, J., Wang, Q., Chen, L., Wu, Q., 2020. Dynamic analysis of the rock burst potential of a longwall panel intersecting with a fault. Rock Mech. Rock Eng. 53, 1737–1754.

Keneti, A., Sainsbury, B., 2018. Review of published rockburst events and their contributing factors. Eng. Geol. 246, 361–373.

Kozłowska, M., Orlecka-Sikora, B., Dineva, S., Rudziński, Ł., Boskovic, M., 2021. What governs the spatial and temporal distribution of aftershocks in mining-induced seismicity: Insight into the influence of coseismic static stress changes on seismicity in Kiruna Mine, Sweden. Bull. Seismol. Soc. Am. 111(1), 409–423.

Kwiatek, G., Plenkers, K., Dresen, G., 2011. Source parameters of picoseismicity recorded at Mponeng Deep Gold Mine, South Africa: Implications for scaling relations. Bull. Seismol. Soc. Am. 101(6), 2592–2608.

Latour, S., Campillo, M., Voisin, C., Ionescu, I., Schmedes, J., Lavallée, D., 2011. Effective friction law for small-scale fault heterogeneity in 3D dynamic rupture. J. Geophys. Res.: Solid Earth 116 (B10), B10306.

Li, Z., Elsworth, D., Wang, C., Im, K., 2019. A new apparatus for the concurrent measurement of friction and permeability evolution in fault gouge. Int. J. Rock Mech. Min. Sci. 121, 104046.

Lu, C., Liu, B., Liu, B., Liu, Y., Wang, H., Zhang, H., 2019. Anatomy of mining-induced fault slip and a triggered rockburst. Bull. Eng. Geol. Environ. 78, 5147–5160.

Luo, B., Duan, B., 2018. Dynamics of nonplanar thrust faults governed by various friction laws. J. Geophys. Res.: Solid Earth 123(6): 5147–5168.

Ma, J., Dong, L., Zhao, G., Li, X., 2018. Discrimination of seismic sources in an underground mine using full waveform inversion. Int. J. Rock Mech. Min. Sci. 106, 213–222.

Martínez-Garzón, P., Kwiatek, G., Bohnhoff, M., Dresen, G., 2016a. Impact of fluid injection on fracture reactivation at The Geysers geothermal field. J. Geophys. Res.: Solid Earth 121(10), 7432–7449.

Martínez-Garzón, P., Vavryčuk, V., Kwiatek, G., Bohnhoff, M., 2016b. Sensitivity of stress inversion of focal mechanisms to pore pressure changes. Geophys. Res. Lett. 43(16), 8441–8450.

Mendecki, M., Szczygiel, J., Lizurek, G., Teper, L., 2020. Mining-triggered seismicity governed by a fold hinge zone: The Upper Silesian Coal Basin, Poland. Eng. Geol. 274, 105728.

Meng, H., Ge, H., Yao, Y., Shen, Y., Wang, J., Bai, J., Zhang, Z., 2022. A new insight into casing shear failure induced by natural fracture and artificial fracture slip. Eng. Failure Anal. 137, 106287.

Orlecka-Sikora, B., Papadimitriou, E., Kwiatek, G., 2009. A study of the interaction among mining-induced seismic events in the Legnica-Głogów Copper District, Poland. Acta Geophys. 57, 413–434.

Petružálek, M., Jechumtálová, Z., Šílený, J., et al., 2020. Application of the shear-tensile source model to acoustic emissions in Westerly granite. J. Rock Mech. Min. Sci. 128, 104246.

Rojas, O., Dunham, E., Day, S., Dalguer, L., Castillo, J., 2009. Finite difference modelling of rupture propagation with strong velocity-weakening friction. Geophys. J. Int. 179(3): 1831–1858.

Sainoki, A., Mitri, H., 2014. Dynamic behaviour of mining-induced fault slip. Int. J. Rock Mech. Min. Sci. 66, 19–29.

Si, G., Cai, W., Wang, S., Li, X., 2020. Prediction of relatively high-energy seismic events using spatial-temporal parametrization of mining-induced seismicity. Rock Mech. Rock Eng. 53, 5111–5132.

Song, C., Lu, C., Zhang, X., Wang, C., Xie, H., Yan, X., Yang, H., 2022. Moment tensor inversion and stress evolution of coal pillar failure mechanism. Rock Mech. Rock Eng. 55 (4), 2371–2383.

Song, J., Lu, C., Song, C., Zhang, X., Wang, Y., Liu, F., Liu Y., 2023. A source mechanism of the mining-triggered tremor in the Xinjulong Coal Mine revealed by the Bayesian inversion and 3D simulation. Rock Mech. Rock Eng, 56(12), 8591–8606.

Toda, S., Stein, R., Sevilgen, V., Lin, J., 2011. Coulomb 3.3 Graphic-rich deformation and stress-change software for earthquake, tectonic, and volcano research and teaching—user guide: US Geol. Surv. Open-File Rep. 1060, 63.

Vasyura-Bathke, H., Dettmer, J., Dutta, R., Mai, P., Jonsson, S., 2021. Accounting for theory errors with empirical Bayesian noise models in nonlinear centroid moment tensor estimation. Geophys. J. Int. 225(2), 1412–1431.

Vasyura-Bathke, H., Dettmer, J., Steinberg, A., et al., 2020. The Bayesian earthquake analysis tool. Seismol. Res. Lett. 91(2A), 1003-1018.

Wang, P., Luan, H., 2022. Size effect analysis of remaining coal pillar on rock burst caused by fault. Bull. Eng. Geol. Environ. 81(3), 108.

Wang, X., Cai, M., 2017a. Numerical analysis of ground motion in a South African mine using SPECFEM3D. In: UMT 2017: Proceedings of the 1st International Conference on Underground Mining Technology. Australian Centre for Geomechanics, Perth, pp. 255–268.

Wang, X., Cai, M., 2017b. Numerical modeling of seismic wave propagation and ground motion in underground mines. Tunn. Undergr. Space Technol. 68, 211–230.

Yildirim, I., 2012. Bayesian inference: Metropolis-hastings sampling. Dept. of Brain and Cognitive Sciences, Univ. of Rochester, Rochester, NY.

Zang, A., Wagner, F., Stanchits, S., Janssen, C., Dresen, G., 2000. Fracture process zone in granite. Int. J. Earth Sci. Eng. 105(B10), 23651–23661.

Zhang, N., Zhang, Z., Shan, R., Qi, Q., Zhao, S., Sun, Z., Guo, Y., 2023. An experimental study of fault slips under unloading condition in coal mines. Bull. Eng. Geol. Environ. 82(4), 126.

Zhang, Q., Zou, J., Wang, J., Jiao, Y., Xu, H., 2024. Mechanism of coal bump induced by joint slipping under static and dynamic stresses in graben structural area. Acta Geotech. 19(1), 347–361.

Zhang, W., Feng, X., Yao, Z., Hu, L., Xiao, Y., Feng, G., Niu, W., Zhang, Y., 2022. Development and occurrence mechanisms of fault-slip rockburst in a deep tunnel excavated by drilling and blasting: a case study. Rock Mech. Rock Eng. 55(9), 5599–5618.

Zhang, Y., Wang, Y., Bai, Y., Li, Y., Lv, Z., Ding, H., 2019. A new rockburst experiment data compression storage algorithm based on big data technology. Intell. Autom. Soft Co. 25(3), 561–572.

Zhou, Q., Liu, D., Lin, X., 2022. Pre-evaluation of fault stability for underground mining based on geomechanical fault-slip analysis. Geomat., Geomat. Nat. Haz. Risk 13(1), 400–413.

Jiefang Song has been enrolled in successive postgraduate and doctoral programs in Mining Engineering at the School of Mines, China University of Mining and Technology since September 2021. He has published four papers as the first author in the esteemed international journals. His research interests focus on two main areas: (1) the understanding of geomechanical-seismological processes in mining-induced seismicity and (2) acoustic emission analysis from laboratory experiments on rock samples.

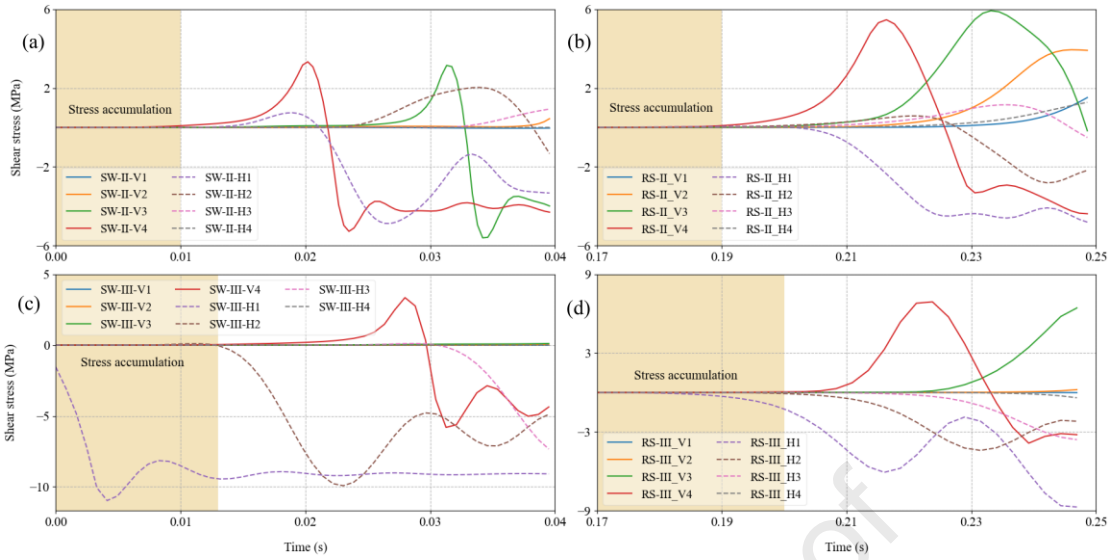

Fig. 10. Stress changes at monitoring locations during dynamic rupture for different model scenarios: (a) slip weakening model with in-plane shear rupture source, (b) rate and state model with in-plane shear rupture source, (c) slip weakening model with out-of-plane shear rupture source, and (d) rate and state model with out-of-plane shear rupture model. The monitoring locations are shown in Fig. 7, where *V* and *H* represent the vertical and horizontal monitoring points, respectively.

Declaration of interests

☒ The authors declare that they have no known competing financial interests or personal relationships that could have appeared to influence the work reported in this paper.

☐The authors declare the following financial interests/personal relationships which may be considered as potential competing interests: